Analysis of Heat Transfer Behaviors in EAGLE ID1 Test Using Particle-Based Simulation Method

Aprianti, Nur Asiah
Department of Applied Quantum Physics and Nuclear Engineering, Kyushu University : Graduate Student

Oshima, Wataru
Department of Applied Quantum Physics and Nuclear Engineering, Kyushu University : Graduate Student

Morita, Akihiro
Department of Applied Quantum Physics and Nuclear Engineering, Kyushu University : Graduate Student

https://hdl.handle.net/2324/1456157

Analysis of Heat Transfer Behaviors in EAGLE ID1 Test
Using Particle-Based Simulation Method

by

Nur Asiah Aprianti[*], Wataru OSHIMA[*], Akihiro MORITA[*] and Koji MORITA[**]

Abstract

In the EAGLE in-pile ID1 test, which has been performed by Japan Atomic Energy Agency (JAEA) to demonstrate early fuel discharge from a fuel subassembly with an inner duct structure (FAIDUS), it was deduced that observed early duct wall failure was initiated by high heat flux from the molten pool of fuel and steel mixture. The posttest analyses suggest that pool-to-duct wall heat transfer might be enhanced effectively by the molten steel in the pool without the presence of fuel crust on the duct wall. In the present study, mechanisms of effective heat transfer from the molten pool to the duct wall was analyzed using a fully Lagrangian approach based on the finite volume particle (FVP) method for multi-component, multi-phase flows. Material distribution as well as steel droplet size in the molten pool after its formation was considered as parametric simulations. The present 2D particle-based simulations demonstrated that large thermal load that leads to early duct wall failure can be caused by local contact of molten steel to the duct wall as well as discrete formation of fuel crust on the duct wall.

Keywords: Core disruptive accidents, Sodium cooled fast reactor, FAIDUS, Particle-based simulation, Finite volume particle method, Molten pool heat transfer

1. Introduction

In the study of postulated core disruptive accidents (CDAs) it has been recognized as an important characteristic of the sodium cooled fast reactors (SFRs) that the intact SFR core is not designed in the maximum reactive configuration. This could cause energetic reactivity excursions due to relocation of core materials or dimensional change of the core during a postulated CDA. In this concern, the FAIDUS (fuel subassembly with an inner duct structure) concept has been proposed for the design of JSFR (Japan Sodium-cooled Fast Reactor) to achieve an early accident

---

[*]   Graduate Student, Department of Applied Quantum Physics and Nuclear Engineering
[**]   Professor, Department of Applied Quantum Physics and Nuclear Engineering

termination before a large-scale fuel pool formation associated with energetic recriticality events[1,2]. This FAIDUS concept is one of the design measures for so-called controlled material relocation (CMR). In FAIDUS, where each fuel subassembly is equipped with an inner duct, it is expected that the early failure of the inner duct wall followed by fuel discharge outside of the active core region through the inner duct. This fuel relocation can prevent the formation of critical molten fuel pool, which has a potential of severe energetics due to excessive fuel cohesion initiated by pool sloshing. Therefore, it is necessary to demonstrate the effectiveness of FAIDUS with the early inner duct wall failure followed by the molten fuel relocation to reduce the power level sufficiently.

An extensive experimental program, the EAGLE (Experimental Acquisition of Generalized Logic to Eliminate recriticalities) project, has been conducted to confirm the capability of early fuel removal using the FAIDUS concept by Japan Atomic Energy Agency (JAEA) at the facilities of IGR (Impulse Graphite Reactor) in National Nuclear Center (NNC) of Kazakhstan[3]. The in-pile large-scale test ID1, which was one of the integral demonstration experiments in the EAGLE project, was intended to generate a molten fuel/steel mixture, which simulated the relatively high-power subassembly under reactor accident conditions. In this test, the molten fuel at the temperature beyond its melting point exposed a duct wall, which simulated the inner duct wall of FAIDUS, to high heat flux of about 10 MW/m^2. The duct wall finally failed following the molten fuel penetration into the relocation path within a short period (~1 s) after its melting even when the duct was initially filled with liquid sodium at around 700 K.

One of the key behaviors observed in the ID1 test is the early duct wall failure caused by high heat flux conditions. Therefore, mechanism of heat transfer from the molten fuel/steel mixture fuel to the duct wall must be well understood to demonstrate the effectiveness of FAIDUS as a design measure for CMR under reactor conditions. The heat transfer characteristics relevant to the duct wall failure have been investigated by integral thermal-hydraulic calculations using a fast reactor safety analysis code, SIMMER-III[4,5]. Although the SIMMER-III calculations might represent macroscopic fluid-dynamics behaviors of multi-component, multi-phase flows involved in the ID1 test reasonably, this code based on the Eulerian method hardly models local and discrete multi-phase flow behaviors involved in a set of heat transfer processes. On the other hand, particle-based simulations based on a fully Lagrangian framework might be one of the promising computational fluid dynamics (CFD) methods to directly simulate multi-component, multi-phase flows without empirical models such as flow regime map and heat-transfer correlations. This method is more appropriate for fluid-fluid and fluid-solid interphase simulations since the interphases can be clearly represented in calculations compared with conventional Eulerian mesh methods.

In this study, the heat transfer characteristics from the molten pool materials to outer surface of inner duct wall observed in the EAGLE ID-1 test were investigated through analyses using the particle-based simulations based on the finite volume particle (FVP) method[6]. Mechanisms of heat transfer with large thermal load to the duct wall as well as fuel crust formation was evaluated through comparison with the experimental data and the posttest analyises[4,5]. Heat transfer characteristics involved in the ID1 test will be also discussed based on a phenomenological consideration.

2.   Overview of ID-1 Test and Posttest Analyses

The ID-1 test simulated a partial molten core region and its surroundings in a reactor core. **Figure 1** shows the schematic of the main test section for the ID1 test. It consisted of the discharge cylindrical duct and the fuel assembly. The duct wall was made of stainless steel with inner

diameter of 40 mm and thickness of 2 mm. The inner duct initially filled with liquid sodium was installed vertically at the central part through the annual structure of a fuel assembly jacket. A 75-pin fuel assembly surrounded the duct in three columns with 400-mm fissile height giving total fuel (UO_2) amount of about 7.1 kg. The test section was inserted into the central experimental channel of the IGR core, and was heated up to around 570 - 670 K first. The nuclear energy was then put into the fuel up to its temperature of about 3,270 K by the high neutron flux from the IGR core. In the test, the duct wall failure was initiated about 1 s after the start of fuel/steel mixture pool formation associated with rapid wall heating. After the wall failure, the main fuel discharge through the inner duct occurred within a short period less than 2 s. The contact of discharged mixture materials with sodium in the duct resulted in rapid sodium vaporization leading to almost complete voiding of the duct channel.
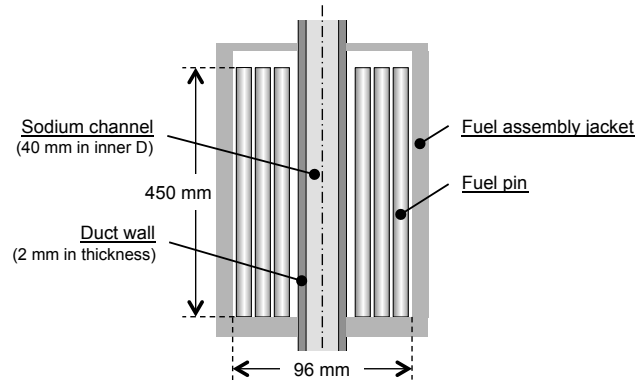

Fig. 1 Schematic of main test section for ID1 test.

To clarify mechanism of the duct wall failure measured in the experiment, the posttest analyses was performed using the TAC2D and SIMMER-III codes[4,5]. First, TAC2D, which is a general-purpose heat conduction code, was used to estimate the wall temperature when the duct wall failure occurred in the test. In this calculation, by reproducing the temperature response locally measured at the inner surface of duct wall, the temperature of duct-wall outer surface was estimated to reach 1,625 K when the duct wall failure occurred in the experiment. It was also deduced that the average heat flux from the start of heat transfer until the duct wall failure was 10.7 MW/m^2. Based on these estimations, integral thermal-hydraulic calculations were then performed to simulate the whole process of ID1 test including the fuel-pin disruption, molten pool formation and duct wall failure behaviors using the SIMMER-III code.

In the SIMMER-III calculations, the ID1 test section of inner duct and fuel assembly was molded in a 2D cylindrical coordinate system. The calculation results indicated that the outermost fuel pins started melting first at 4.2 s after the start of energy insertion into the test fuel. The following other fuel-pin disruption formed a fuel/steel mixture pool. Fuel crust formation on the colder duct wall surface was predicted to occur mostly in the lower pool region at the early stage of fuel melting. This built a thermal resistance layer suppressing the heat transfer from the mixture materials to the duct wall. On the other hand, in the upper pool region, the duct wall surface was exposed directly by the molten steel with rather high thermal conductivity. As a result, in the SIMMER-III calculation, the duct wall failure, which was defined to occur when the duct wall surface temperature reached 1,625 K according to the TAC2D estimation, was predicted at 0.7 s after the start of the pool-wall heat transfer. This early failure timing is comparable with the experimental result. In the calculation, the average heat flux from the start of heat transfer until the duct wall failure was about 10 MW/m^2 at the wall failure location. Such high heat flux, which is consistent with the TAC2D result, might be enhanced by a relatively larger faction of molten steel,

which accumulated in the upper pool region due to density difference between fuel and steel.

3. Particle-based Simulation Method

3.1 Finite volume particle method

In the present study, multi-component, multi-phase flow phenomena with heat and mass transfer, which were involved in the EAGLE ID1 test, were analyzed by a fully Lagrangian approach based on the FVP method. The governing equations to be solved are the following Navier-Stokes equation, the continuity equation and the energy equation for incompressible fluids:

$$\rho \frac{D\bar{u}}{Dt} = -\nabla p + \nabla(\mu\nabla \cdot \bar{u}) + \bar{f} \tag{1}$$

$$\nabla \cdot \bar{u} = 0 \tag{2}$$

$$\rho \frac{DH}{Dt} = \nabla \cdot (k\nabla T) + Q \tag{3}$$

where ρ is the density, $\bar{u}$ is the velocity, t is the time, p is the pressure, μ is the dynamic viscosity, H is the specific enthalpy, k is the thermal conductivity and T is the temperature. The third term $\bar{f}$ in the right-hand side of Eq. (1) represents other forces per unit volume, such as surface tension and gravity. The second term Q in the right-hand side of Eq. (3) includes the heat transfer rate at the interface between different phases and the nuclear heat per unit volume.

In the FVP method, the calculation domain is represented by a set of discrete numerical particles, which are not only the interpolation points, but also carry the material properties. The velocity and energy of each particle are calculated through interactions with neighboring particles covered with a kernel function. All terms in the governing equations, such as gradient and Laplacian terms, are discretized using a deterministic particle interaction model, which will be simply introduced in the following. A detailed review of the FVP method can be found in our pervious study[7].

The numerical particles are assumed to occupy a certain volume, where the control volume of one moving particle is a circle in 2D simulations:

$$S = 2\pi R , \quad V = \pi R^2 = (\Delta l)^2 \tag{4}$$

where S, V, R and Δl are the particle surface area, the particle control volume, the radius of particle control volume and the initial particle distance, respectively. According to Gauss's law, the gradient and Laplacian operators acting on an arbitrary scalar function ϕ can be approximated as

$$\langle \nabla\phi \rangle_i = \left\langle \frac{1}{V}\oint_S \phi\bar{n}\,dS \right\rangle_i = \frac{1}{V}\sum_{j\neq i}\phi_{sur}\cdot\bar{n}_{ij}\cdot\Delta S_{ij} \tag{5}$$

$$\langle \nabla^2\phi \rangle_i = \left\langle \frac{1}{V}\oint_S \nabla\phi\cdot\bar{n}\,dS \right\rangle_i = \frac{1}{V}\sum_{j\neq i}\left(\frac{\phi_j - \phi_i}{|\bar{r}_{ij}|}\right)\cdot\Delta S_{ij} \tag{6}$$

where $\langle\phi\rangle_i$ is the approximation of ϕ with respect to particle i and $|\bar{r}_{ij}|$ is the distance between particles i and j, and $\bar{n}$ is the unit vector. The function value ϕ_{sur} on the surface of particle i can be evaluated using a linear function as

$$\phi_{sur} = \phi_i + \frac{\phi_j - \phi_i}{|\vec{r}_{ij}|} R \tag{7}$$

The unit vector $\bar{n}_{ij}$ of distance between particles i and j is defined as

$$\vec{n}_{ij} = \frac{\vec{r}_{ij}}{|\vec{r}_{ij}|} = \frac{\vec{r}_j - \vec{r}_i}{|\vec{r}_{ij}|} \tag{8}$$

The interaction surface ΔS_{ij} between particles i and j can be calculated as

$$\Delta S_{ij} = \frac{\omega_{ij}}{\sum_{j \neq i} \omega_{ij}} S \tag{9}$$

where ω_{ij} is the kernel function defined as

$$\omega_{ij} = \begin{cases} \sin^{-1}\left(\dfrac{R}{|\vec{r}_{ij}|}\right) - \sin^{-1}\left(\dfrac{R}{r_e}\right) & |\vec{r}_{ij}| \leq r_e \\ 0 & |\vec{r}_{ij}| > r_e \end{cases} \tag{10}$$

where r_e is the cut-off radius, which is chosen as $4.1\Delta l$ for 2D systems. This cut-off radius is used to define the limitation area of neighboring particles around particle i. The fluid movement and phase changes are modeled through these neighboring particle interactions. The gradient and Laplacian operators, which are given by Eqs. (5) and (6), respectively, are then solved using the combined and unified procedure (CUP) algorithm, which is explained in detail in our previous study[8].

3.2 Heat and mass transfer model

In the present study, the heat and mass transfer processes of materials were modeled as non-equilibrium and equilibrium transfers as well as heat conduction. Phase changes occurring at interfaces between two different materials or between two different phases are represented by a non-equilibrium process because the bulk conditions of a particle are generally not at the phase-change temperature when the mass transfer occurs at the interface[9]. On the other hand, the equilibrium process of melting or freezing occurs when the bulk energy of the phase satisfies the phase-change condition[8]. In this section, the non-equilibrium model to represent the possible interfacial heat and mass transfer processes involved in the ID1 test is described in detail.

The second term in the right-hand side of Eq. (3) is expressed to represent the non-equilibrium transfers and nuclear heating as follows:

$$Q = Q^h + Q^m + Q^n \tag{11}$$

where Q^h is the heat transfer rate per unit volume at the interface, where phase change can occur, Q^m is the energy transfer rate per unit volume due to phase change, and Q^n is the volumetric heat source due to nuclear heating.

3.2.1 Interfacial heat transfer

The term Q^h is modeled to calculate the heat transfer at the interface between particles with different materials or phases. The heat transfer rate from the interface between particles i and j to particle i is formulated as

$$Q_{i,j}^{\mathrm{h}} = a_{ij} h_i (T_{ij}^{\mathrm{I}} - T_i) \tag{12}$$

where a_{ij} is the heat transfer area per unit volume between particle i and j, h_i is the heat transfer coefficient of particle i, and T_{ij}^{I} is the temperature of the interface between particles i and j. For particle i, the term Q^{h} of Eq. (11) is calculated as

$$[Q^{\mathrm{h}}]_i = \sum_{j \neq i} Q_{i,j}^{\mathrm{h}} \tag{13}$$

Although h_i should be modeled so as to represent effective heat transfer depending on flow conditions, it is simply approximated as

$$h_i = \frac{2k_i}{\Delta l} \tag{14}$$

where k_i is the thermal conductivity of particle i.

The interface temperature T_{ij}^{I} should be the phase change temperature when occurrence of phase change is predicted at the interface. If particles i and j consist of the same material, T_{ij}^{I} can be expressed by

$$T_{ij}^{\mathrm{I}} = \min[T_{\mathrm{Liq},\mathrm{M}(i)}, \max(T_{ij}^{\mathrm{N}}, T_{\mathrm{Sol},\mathrm{M}(i)})] \tag{15}$$

where $T_{\mathrm{Sol},\mathrm{M}(i)}$ and $T_{\mathrm{Liq},\mathrm{M}(i)}$ are the solidus and liquidus temperatures of the material that constitutes of particle i, respectively, and T_{ij}^{N} is given by

$$T_{ij}^{\mathrm{I}} = T_{ij}^{\mathrm{N}} \equiv \frac{h_i T_i + h_j T_j}{h_i + h_j} \tag{16}$$

Equation (16) represents the temperature of the interface where no phase change occurs. For the interface between different materials, an alternative phase change occurring at its interface can be also considered. If we assume that either freezing or melting is dominant at the interface between different materials, T_{ij}^{I} is defined as

$$T_{ij}^{\mathrm{I}} = \max[T_{ij}^{\mathrm{N}}, T_{\mathrm{Sol},\mathrm{M}(i)}] \qquad \text{for freezing} \tag{17}$$

$$T_{ij}^{\mathrm{I}} = \min[T_{ij}^{\mathrm{N}}, T_{\mathrm{Liq},\mathrm{M}(i)}] \qquad \text{for melting} \tag{18}$$

Otherwise, phase change is suppressed at this interface by always assigning

$$T_{ij}^{\mathrm{I}} = T_{ij}^{\mathrm{N}} \tag{19}$$

3.2.2 Non-equilibrium mass transfer

The net heat flow rate at the interface is given by

$$Q_{ij}^{\mathrm{I}} = Q_{i,j}^{\mathrm{h}} + Q_{j,i}^{\mathrm{h}} \tag{20}$$

Once Q_{ij}^{I} is determined, the melting/freezing rate can be calculated. If $Q_{ij}^{\mathrm{I}} > 0$ and the particle i contains liquid phase, it will freeze partly into the solid phase. Its freezing rate per unit volume is calculated by

$$\Gamma_{freezing,i} = \sum_{j \neq i} \frac{Q_{ij}^{\mathrm{I}}}{H_{\mathrm{f},\mathrm{M}(i)}} \tag{21}$$

where $H_{\mathrm{f,M}(i)}$ is the specific latent heat of fusion. If $Q_{ij}^{\mathrm{l}} < 0$ and the particle i contains solid phase, it will melt partly into the liquid phase. Its melting rate per unit volume is calculated by

$$\Gamma_{melting,i} = -\sum_{j \neq i} \frac{Q_{ij}^{\mathrm{l}}}{H_{\mathrm{f,M}(i)}} \tag{22}$$

Otherwise only sensible heat will be exchanged for the particle i by applying T_{ij}^{N} to the interface. As a result, to conserve the energy of particle i, the term Q^{m} of Eq. (11) should be expressed by

$$[Q^{\mathrm{m}}]_i = \sum_{j \neq i} Q_{i,j}^{\mathrm{h}} = \sum_{j \neq i} (\Gamma_{melting,i} - \Gamma_{freezing,i}) H_{\mathrm{f,M}(i)} \tag{23}$$

3.2.3 Crust formation model

The fuel crust formation on the steel wall could deteriorate the heat transfer from the molten pool to the duct wall due to low thermal conductivity of crust fuel. To model this effect reasonably, at the liquid fuel/steel wall and liquid fuel/fuel crust interfaces, considering the thickness of solid crust formed on the duct wall, the heat transfer coefficient of liquid fuel side is calculated instead of Eq. (14) by

$$h_i = \left[\frac{\min(\delta_i, \Delta l/2)}{k_{\mathrm{S}}} + \frac{\Delta l/2 - \min(\delta_i, \Delta l/2)}{k_{\mathrm{L}}} \right]^{-1} \tag{24}$$

where k_{S} and k_{L} are the thermal conductivity of solid and liquid fuel, respectively. The crust thickness of particle i is defined by

$$\delta_i = \frac{m_{\mathrm{S},i}}{m_i} \Delta l \tag{25}$$

where m_i and m_{S} are the total and solid masses of particle i, respectively.

3.3 Viscosity and buoyancy models

The rheological behavior in melt under melting and freezing has obvious influence on solid and fluid dynamics. In the present study, it was considered as change in viscosity of melt as a function of melt enthalpy based on our previous works[8,9]. Natural convection flows in the sodium channel and the molten pool, which are driven by the buoyancy force, were considered by the Boussinesq approximation for the gravity term involved in $\bar{f}$ of Eq. (1):

$$\bar{f}_g = \rho[1 - \beta(T - T_0)]\bar{g} \tag{26}$$

where $\bar{g}$, β and T_0 are the gravity, the volumetric thermal expansion coefficient and the reference temperature, respectively.

Shirakawa et al.[10] suggested that particle methods would underestimate the buoyancy force caused by density deference between two phases, and introduced a correction term for buoyancy into the pressure gradient term. In the present study, a similar idea is applied by adding a correction term to Eq. (1). For particle i, the modified buoyancy term is calculated as follows:

$$\bar{f}_{g,i} = \rho_i[1 - \beta_i(T_i - T_0)]\bar{g} - \sum_{i \neq j} c_{\mathrm{B}}(\rho_j - \rho_i)\bar{g}\omega_{ij} \tag{27}$$

where c_{B} is the adjustable parameter. In the present study, the value of c_{B} was determined based on a specific test calculation of a single steel droplet rising in a stagnant liquid UO_2 pool. The test calculation demonstrated that the modified buoyancy term with $c_{\mathrm{B}} = 0.01$ is effective to

reproduce the droplet terminal velocity, which can be evaluated by an empirical correlation[11], accurately.

4.   Particle-Based Simulations of ID1 Test

4.1 Modeling of ID1 test conditions
4.1.1 Phase change processes

In the present study, to analyze heat transfer characteristics from the molten pool materials to the outer surface of inner duct wall in the ID-1 test, the molten pool simulations, which initially start the calculation from a molten pool condition, were performed using the particle-based method. It was assumed that the molten pool can consist of molten fuel, molten steel and solid fuels including crust formed on the duct wall surface. The heat will be transferred from the molten pool to the sodium through the steel duct wall.

In the present simulations, the phase changes after the molten pool formation were modeled by the non-equilibrium model as well as the conventional equilibrium phase-change model[8]. **Table 1** shows the non-equilibrium phase changes calculated in the present molten pool simulations. Seven binary interfaces were considered among liquid and solid fuel, liquid steel, steel wall and sodium. At the interfaces between different materials, liquid fuel/liquid steel and liquid fuel/steel wall contacts, fuel freezing was assumed dominant. Although, at the latter interface, both fuel freezing and steel wall melting are possible to occur, it was considered that the effect of crust formation on the steel wall on pool-wall heat transfer should be identified by the crust formation model with the non-equilibrium phase change model. Interface temperatures are defined based on the model formulas for interfacial heat transfer described in Section 3.2. **Figure 2** presents the possible phase changes modeled as non-equilibrium transfers in the present molten pool simulations.

Table 1 Non-equilibrium phase changes modeled in molten pool simulation.

| Interface	Dominant phase change	Interface temperature
• Liquid fuel/liquid steel	Fuel freezing	Eq. (17)
• Liquid fuel/solid fuel	Fuel melting and freezing	Eq. (15)
• Liquid fuel/steel wall	Fuel freezing (crust formation)	Eq. (17)
• Liquid steel/solid fuel	No phase change	Eq. (19)
• Liquid steel/steel wall	Steel melting and freezing	Eq. (15)
• Solid fuel/steel wall	No phase change	Eq. (19)
• Steel wall/sodium	No phase change	Eq. (19)
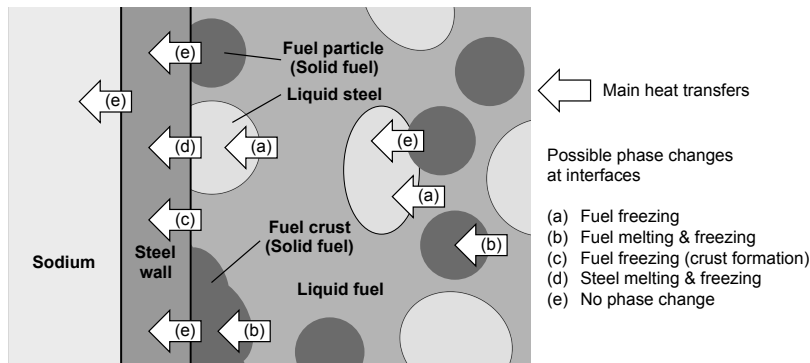
Fig. 2 Possible phase changes modeled as non-equilibrium transfers.

4.1.2 Geometrical conditions

According to discussion on experimental results, which show that the duct wall failure occurred by less than 1 s after the fuel and steel materials started melting, the molten pool calculations were performed for 1 s from the molten pool mixture under several conditions. Since in the present simulations the initial conditions were different from those of the ID-1 test, we performed 2D calculations based on equivalent geometrical conditions for the molten pool, the duct wall and the sodium channel after the start of molten pool-duct wall heat transfer. **Figure 3** shows the schematic of the geometrical conditions used in the present molten pool simulation.

Main physical phenomena to be simulated were heat transfer from the molten pool to the sodium channel through the duct wall, heat transfer among pool materials, and molten fuel freezing on the duct wall as solid crust. In the present simulations, the initial particle distance Δl was set at 1.0 mm, and the time step size was chosen as 1.0×10^{-4} s. We assumed adiabatic geometrical boundaries, neglecting the effect of heat transfer from the system to surroundings. This might be acceptable for a short period time of the present simulations. In the following discussion, time zero corresponds to the start of the molten pool-duct wall heat transfer.
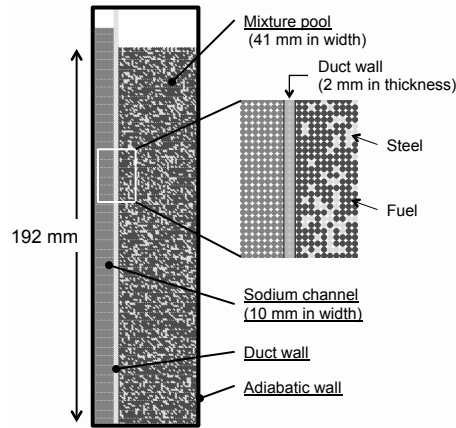

Fig. 3 Geometrical conditions for molten pool simulation.

Table 2 shows the calculation conditions for the present molten pool simulation of the ID-1 test. The experimental geometry was represented by an x-z Cartesian system with a mixture pool of 192 mm in height, which is equivalent to the height of disrupted 75-pins in the annual volume with 26-mm width. The width of the pool region in the calculations was determined based on the ratio of contact area between the mixture pool and the duct wall to the mixture volume. Although the resultant pool width of 41 mm is different from the experimental one, an equivalent thermal load to the duct wall, which is induced by the mixture pool, can be represented approximately using the same volume of the pool mixture per unit area of the duct wall as that in the experiment. The hydraulic diameter of the sodium channel (10 mm) was taken from the experimental condition. In the ID1 test, adequate nuclear power to the fuel in the test section was given to form the fuel/steel mixture pool by the power pulse transient of IGR. In the present simulations, we used the total nuclear heat to the fuel equivalent to that of the ID-1 test after the mixture pool formation. It was assumed that the average nuclear heating rate per unit fuel volume is given as the following linear function of time approximately:

$$Q^n \ [\text{W/m}^3] = 1.15 \times 10^9 (t + 4.2) \tag{28}$$

where t [s] is the time after the start of the molten pool-duct wall heat transfer. In the simulations,

Eq. (28) was included in the term Q of the energy equation, Eq. (3). The axial and lateral nuclear power profiles were also considered based on the experiment. The initial conditions of the pool mixture will be discussed later.

In the posttest analysis[4,5], it was discussed that the presence of steel in the mixture pool played key roles in quite high heat flux to the duct wall, which might lead to the early wall failure. Therefore, it is of importance to clarify which pool conditions can contribute to the thermal load to the duct wall with high heat flux. In the present study, several initial conditions of the duct wall contact to the mixture pool, fuel crust formation on the duct wall, and steel droplet size were considered as the key parameters, which could have a large impact on the thermal load to the duct wall.

Table 2 Conditions of molten pool simulation.

Mixture pool		
Height × Width [mm]		192×41
Total volume [m^3]		7.87×10^{-3}
(Fuel) [m^3]		5.91×10^{-3}
(Steel) [m^3]		1.96×10^{-3}
Total mass [kg]		70.8
(Fuel) [kg]		56.6
(Steel) [kg]		14.2
Duct wall		
Thickness [mm]		2.0
Initial temperature [K]		720
Sodium channel		
Width [mm]		10
Initial temperature [K]		720

4.1.3 Molten pool conditions

The history of nuclear energy generation in the fuel of the ID1 test suggests that the total energy input into the fuel by the start of molten pool-wall heat transfer was just about the energy necessary to heat the fuel up to the enthalpy at its liquidus temperature[12]. This energy should be expended not only to melt the fuel pellets and steel claddings of the pins, but also to increase their temperatures as well as those of the duct wall and the sodium. Therefore, in the present simulations, it was roughly assumed that the mixture pool consisted of fuels in liquid and solid phases, and steel in liquid phase at the start of the pool-wall heat transfer. Here, we considered three cases of initial solid-fuel temperature, 1,750 K, 2,250 K and 2,500 K, to specify the mass fraction of solid phase in the fuel. In addition, we assumed that the temperatures of molten fuel and steel were 3,150 K and 1,750 K, respectively, which are just beyond their melting points, when the mixture pool was formed. By simple energy balance calculations using appropriate thermophysical properties of fuel and steel[13], we obtained the initial conditions of solid fuel in the mixture pool as shown in **Table 3**. It can be seen that the solid fuel occupies almost half of the fuel mass in the mixture pool even if we assume that the temperature of solid fuel is the same as that of molten steel. In addition, transient molten-pool calculations under these initial conditions showed that there is no remarkable difference in average temperature increase of the mixture pool among the three cases. Therefore, hereafter, we took the mass fraction 47% of solid phase at 1,750 K in fuel as a reference condition.

Table 3 Initial conditions of solid fuel in mixture pool.

Temperature of solid fuel	Mass fraction of solid phase in fuel
1,750 K	0.47
2,250 K	0.59
2,500 K	0.69

4.2 Molten pool simulations
4.2.1 Effect of fuel crust

In the posttest analyses[4,5], time variations of duct-wall surface temperature on the pool side were predicted by the SIMMER-III code. The results indicated that the crust formation on the duct wall surface deteriorated the pool-wall heat transfer largely. In the present study, to find the typical initial pool conditions from the viewpoint of pool-wall heat transfer, the local temperature of duct wall surface predicted by the SIMMER-III code was compared with those calculated by the present particle-based simulation. Although the initial pool compositions were determined based on the above discussion, we simply considered a homogeneous mixture of solid fuel, liquid fuel and liquid steel with initial random arrangement. Two parametric cases were calculated to preliminarily know the characteristics of pool-wall heat transfer. One case assumed the surface of the duct wall initially contacting the homogeneous fuel/steel mixture directly, and the other was the duct wall surface covered by the fuel crust with thickness of 1 mm. Hereafter, these calculations are called the cases of pool mixture contact and fuel crust contact, respectively. In the former case, about 25% of the duct-wall surface contacted the molten steel according to the volume faction of steel in the pool.

Figure 4 shows the two calculation results of duct-wall surface temperature in comparison with the result predicted by the SIMMER-III code[5], which was obtained as the temperature of duct wall surface covered by re-frozen fuel crust. Here, in the present calculations, the duct-wall surface temperatures were evaluated by extrapolating the inside temperatures of the duct wall to the depth of 0.2 mm from the duct surface facing to the pool at the axial position of 100 mm from the pool bottom. This definition of duct-wall surface temperature is consistent with that in the SIMMER-III calculation. It can be seen that the time variation of duct-wall surface temperature in the case of fuel crust contact reasonably agrees with the SIMMER-III prediction after the start of molten pool-wall heat transfer ($t = 0$), although the crust thickness of 1 mm was specified arbitrarily. On the other hand, in the case of pool mixture contact, the temperature change is overestimated due to relatively higher thermal conductivity of molten steel. The present result suggests that some fuel crust might be formed on the duct-wall surface when the duct-wall heat transfer was initiated.
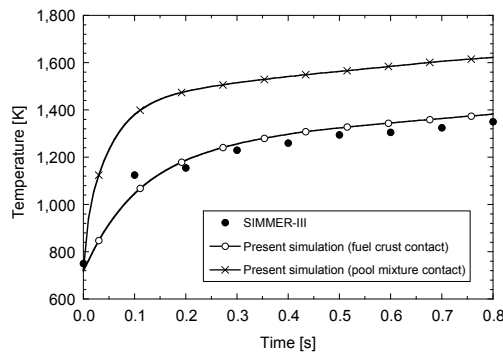

Fig. 4 Duct-wall surface temperature after the start of pool-wall heat transfer.

Figure 5 indicates the axial distributions of heat flux through the duct wall at 0.1 s, 0.3 s, 0.5 s and 0.7 s in the cases of pool mixture contact and fuel crust contact, respectively. Here, they were graphed using the average heat fluxes for every 2.0 cm axial length along the duct wall. The heat flux obtained in the case of fuel crust contact is fairly smaller than that at the duct wall failure, which was predicted to be more than 10 MW/m^2 by the calculations using TAC2D and SIMMER-III[5]. On the other hand, the case of pool mixture contact shows larger heat flux due to good pool-wall heat transfer. As suggested by the posttest analysis[5], during the pool formation process after the pin disruption, the phase separation between fuel and steel materials can occur in their mixture pool due to their density difference. In addition to the crust formation on the duct wall surface, this effect might also play a key role in heat transfer from the pool to the duct wall due to the difference in thermal conductivity between fuel and steel. Therefore, in the present study, we assumed that the steel material accumulates more in the upper pool region due to its smaller density, while it was considered that the fuel crust was formed on the duct-wall surface in the lower pool region during the early stage of pool-wall heat transfer. Based on this idea, in the following simulations, the mixture pool was divided into two regions, the upper steel-rich region and the lower fuel rich region, in which the fuel crust was formed initially on the duct wall surface.
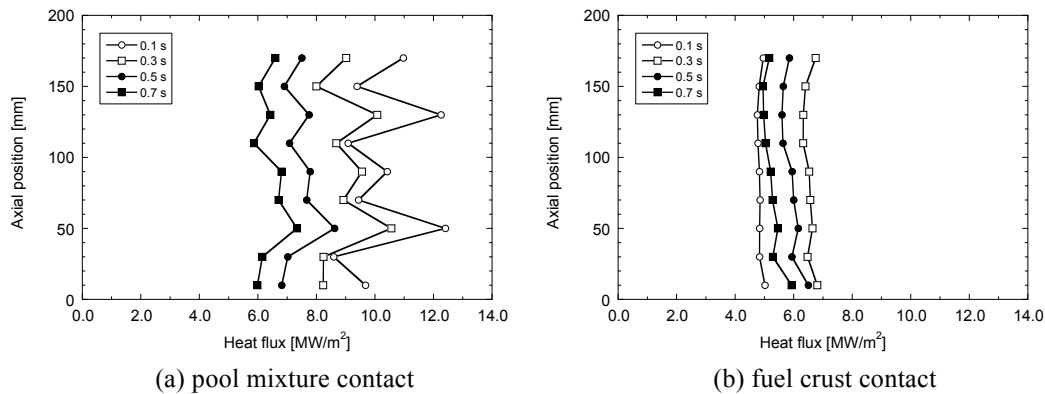

(a) pool mixture contact   (b) fuel crust contact

Fig. 5 Axial distributions of spatial average heat fluxes in the cases of pool mixture contact and fuel crust contact.

4.2.2 Effect of molten steel on pool-wall heat transfer

In the present simulations, the heights of the lower and upper pool regions were arbitrarily defined as 130 mm and 62 mm, respectively. The duct-wall surface in the lower pool region was covered by the fuel crust of 1 mm in thickness. To consider the effect of steel fraction in the mixture pool on the pool-duct wall heat transfer, at first we performed four parametric calculations using different steel fractions. **Table 4** shows the volume fractions of molten steel in the upper and lower pool regions for the four cases, Cases A, B, C and D. We assumed that in the upper pool region the molten steel was mixed with the fuel in one-third of the volume in Case A, and two-third in Case B. For the lower pool region, the volume fraction of steel was also varies among the cases since the total volumes of the fuel and steel in the pool were kept at constant. In Cases A and B, the area fractions of liquid steel-wall contact were nearly identical to the volume fractions of molten steel in the upper pool regions, while only the fuel crust contacted the duct wall in the lower pool region. **Figure 6** indicates the initial material configurations in Cases A and B. On the other hand, in Cases C and D, the duct wall surface in the upper pool region initially contacted the molten steel at the area fraction of 70% and 30%, respectively. These intentional fractions in Cases C and D

were similar to those in Cases B and A, respectively. It is noted that initial material fractions in the upper- and lower-pool regions in Cases C and D were the same as those in Cases A and B, respectively. These two cases were calculated to investigate the effect of the local steel-wall contact on the pool-wall heat transfer. A homogeneous mixture of solid fuel, liquid fuel and liquid steel was specified with initial random configuration except for the pool adjacent to the wall in Cases C and D. The other initial conditions of mixture materials were the same as those considered in the previous discussion.

Table 4 Molten steel fractions in upper and lower pool regions.

	Upper pool region		Lower pool region
	Volume fraction of molten steel	Area fraction of molten steel-wall contact	Volume fraction of molten steel
	[%]	[%]	[%]
Case A	33	33	21
Case B	66	68	4
Case C	33	70	21
Case D	66	30	4
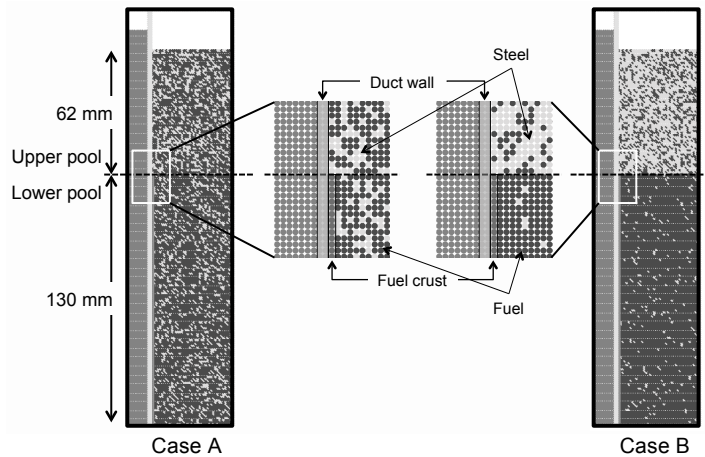
Fig. 6 Initial material configurations in Cases A and B.

In **Fig. 7**, the calculation results on the average temperatures of molten fuel and steel in the mixture pool are compared with those of SIMMER-III[5]. The molten fuel temperature increases are slow because the nuclear heat in the fuel is consumed to heat up and melt the solid fuel, which occupies about half of fuel initially. In the SIMMER-III calculation, the molten steel temperature increases rapidly at around 0.65 s due to development of whole mixing of fuel and steel in the pool after all of the pins disrupted finally. This cannot be represented by the present molten pool simulation on the assumption of the initial homogeneous fuel/steel mixture. Nevertheless, the present simulations show reasonable results on the average temperature increases of the mixture pool in comparison with the SIMMER-III results.

Figure 8 shows the axial distribution of heat flux through the duct wall at 0.1 s, 0.3 s, 0.5 s and 0.7 s after the start of pool-wall heat transfer in Cases A and B. In both cases, the duct wall is exposed by higher heat flux in the upper pool region, and the highest heat flux in Cases A is smaller than that in Case B, where the initial steel volume fraction is twice larger than that in Case

A. In addition, in both cases, the highest heat flux appears in the early stage of heat transfer due to initial large temperature difference between the pool and the wall. On the other hand, the pool-wall heat transfer in the lower pool region with fuel crust on the duct wall is fairly smaller than that in the upper pool region relatively.
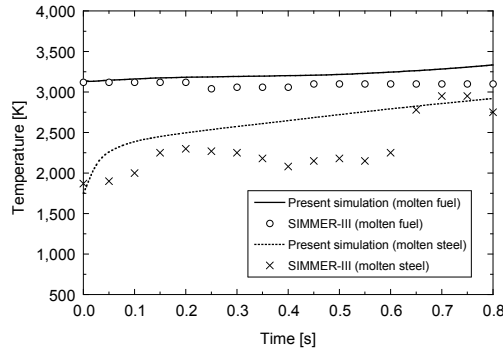

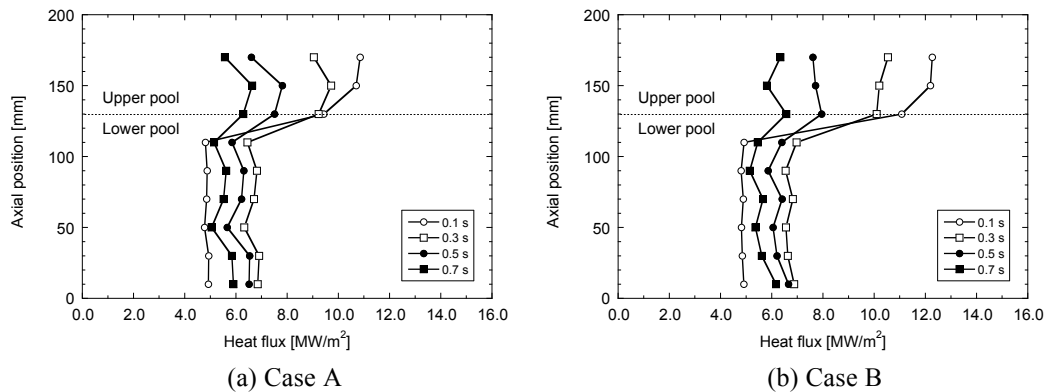**Fig. 7** Time variations of average temperatures of molten fuel and steel in Case A.

Fig. 8 Axial distributions of spatial average heat flux in Cases A and B.

The time variations of averaged heat fluxes over the upper and lower pool regions in Cases A and B are indicated in **Fig. 9**. It can be seen that the duct wall in the upper pool region is exposed to quite high heat flux more than 10 MW/m^2 during the early stage of pool-wall heat transfer. As the duct wall temperature increases, the heat flux decreases gradually. The time-averaged heat flux in the upper and lower pool regions are 9.5 MW/m^2 and 10.4 MW/m^2 in Cases A and B, respectively, during the first period of 0.3 s. These values are good agreement with the result predicted by the SIMMER-III code[5].

The axial heat-flux distributions in Cases C and D are presented in **Fig. 10**. In these cases, the heat fluxes in upper pool region also exceed 10 MW/m^2 during the early stage of pool-wall heat transfer. However, in Case C, regardless of smaller molten-steel concentration in the upper pool, the heat flux there is larger than that in Case D. **Figure 11** shows the comparison of the time variations of averaged heat fluxes over the upper pool region among Cases A, B, C and D. The result of Case C indicates very high heat flux of about 13 MW/m^2 around 0.14 s, although its upper pool has half the amount of molten-steel compared with that in Case B. On the other hand, Cases A and D show similar lower heat flux change. Considering the difference in initial duct surface area contacting the molten steel, these results suggest that the amount of molten steel in the pool has less

influence on the duct-wall heat flux, while the thermal load induced by the molten pool strongly depends on local molten-steel/duct-wall contact. As a matter of course, the larger the steel volume fraction, the larger the steel-wall contact area.
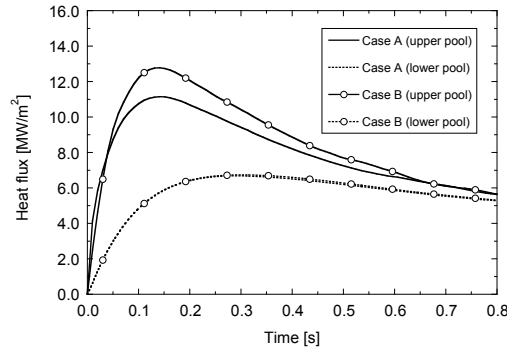

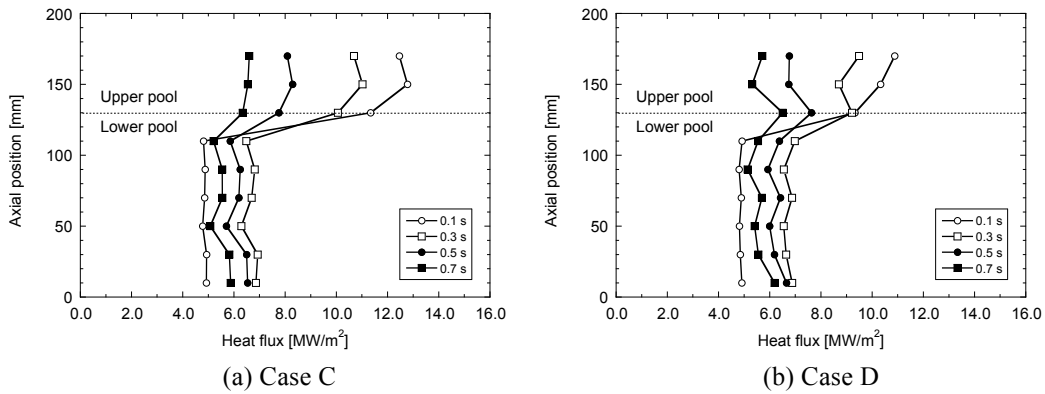**Fig. 9** Time variations of upper- and lower-pool heat fluxes in Cases A and B.

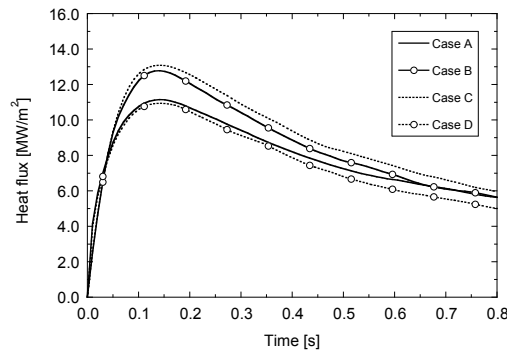**Fig. 10** Axial distributions of spatial average heat fluxes in Cases C and D.

Fig. 11 Comparison of upper-pool heat fluxes among Cases A, B, C and D.

4.2.3 Crust formation behavior

In all of the parametric cases to investigate the effect of molten steel on pool-wall heat transfer, as explained above, the duct wall in lower pool region was intentionally covered by the fuel crust with initial thickness of 1 mm. This condition was based on the discussion with SIMMER-III results[5], where more fuel accumulated in the lower pool region after the molten pool formation.

Since the melting point of fuel is much higher than that of steel, the molten fuel can solidify first on the cold duct wall surface by time and spatial variation. In the present study, this fuel crust formation behavior was modeled by the crust formation model, as explained in Section 3.2.

Figure 12 shows the axial distribution of local crust thickness at 0.3 s in Cases A and B. After the start of pool-wall heat transfer, the fuel crust with initial thickness of 1 mm grows in the lower pool regions, while the new crust is formed even in the upper pool region locally and discretely. In Case B, the crust formation is rather sparse in the upper pool region due to a larger fraction of molten steel, and hence the molten steel can contact larger area of the duct wall surface directly in comparison with Case A. This direct molten-steel contact should enhance the pool-wall heat transfer in the upper pool region.
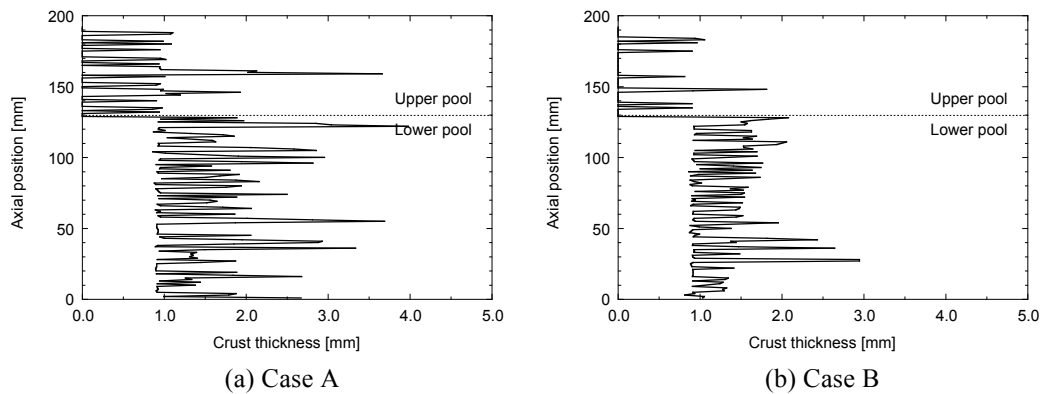

(a) Case A   (b) Case B

Fig. 12 Axial distributions of local crust thickness at 0.3 s in Cases A and B.

In **Fig. 13**, the axial distributions of spatial-average crust thickness are presented at 0.1 s, 0.3 s, 0.5 s and 0.7 s in Cases A and B. Here, they were evaluated as the average thickness for every 2.0 cm axial length along the duct wall. In the lower pool region the fuel crust grows rapidly, while remarkable crust growth cannot be seen in the upper region. In addition, the comparison between Cases A and B indicates that the crust growth rate depends on the fraction of molten fuel in the pool. These crust formation on the duct wall surface could deteriorate the molten pool-duct wall heat transfer, and the present results on the crust behavior are consistent with the resultant heat flux in Cases A and B, which are shown in **Fig. 8**.
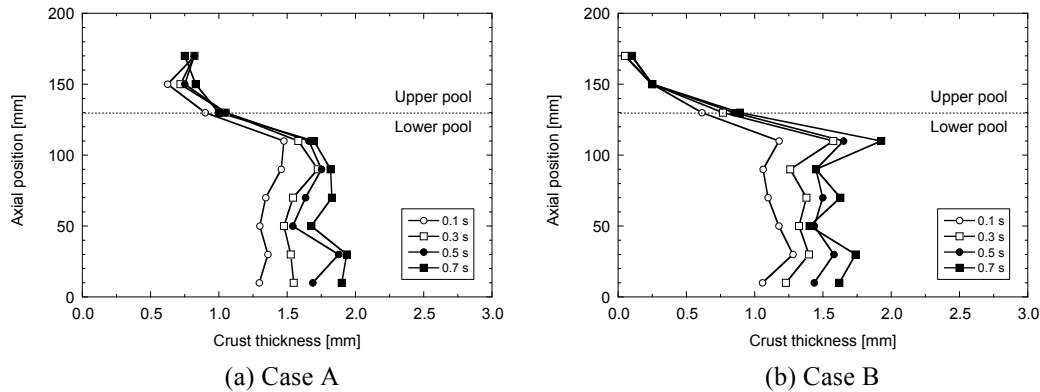

(a) Case A   (b) Case B

Fig. 13 Axial distributions of spatial-average crust thickness in Cases A and B.

The time variations of averaged crust thickness over the upper and lower pool regions in Cases A and B are indicated in **Fig. 14**. It can be seen that the fuel crust gradually becomes thicker in the lower pool region, while in the upper pool region the crust growth almost stagnates. These crust growth behaviors might arise from the difference of fuel fraction adjacent to the crust formed on the duct wall. As can be seen in **Figs. 12**, **13** and **14**, in the lower pool region, the crust growth in Case A is much larger than that in Case B, although the smaller fraction of molten fuel in the lower pool region in Case A. This is because larger nuclear heat in the lower pool region makes the pool temperature higher.
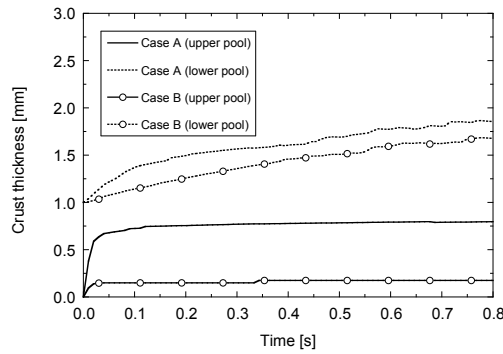

Fig. 14 Time variations of upper- and lower-pool crust thickness in Cases A and B.

4.2.4 Duct wall failure

In the ID1 test, the early duct wall failure was observed at about 0.7 s after the start of the melt contact to the duct wall under the high heat flux of about 10 MW/m^2. In the posttest analysis using the TAC2D code[5], it was deduced that the duct wall failure might occur when the surface temperature of duct wall reached 1,625 K, and the SIMMER-III calculation with this criterion showed a consistent result with the experimental one on the timing of wall failure.
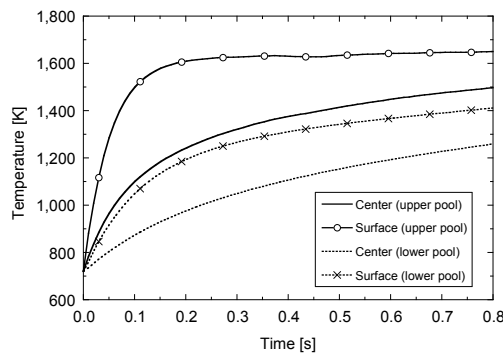

Fig. 15 Time variations of duct wall temperatures in Case C.

Figure 15 indicates the results of Case C on the duct wall temperatures at the pool-side surface and at the center of wall thickness in the upper and lower pool regions. The temperatures in the lower and upper pool regions were evaluated as the temperature averaged over the axial length of 2.0 cm along the duct wall at 5.0 cm and 15.0 cm above the pool bottom, respectively. In the lower pool region, the temperature increases are slower than those in the upper pool due to thermal resistance of fuel crust on the duct wall. On the other hand, the duct-wall surface temperature in the

upper pool region increases rapidly due to large heat transfer during the early transient, and reaches to 1,625 K at 0.27 s after the start of the pool-wall heat transfer. This rapid temperature increase was caused by the direct contact of molten steel to the duct wall as well as discrete formation of fuel crust on the duct wall in the upper pool region. In the present molten pool simulations, we assumed the instantaneous mixture pool formation as an initial condition, and hence the wall failure timing cannot be compared with the experimental result directly. However, based on the experimental fact that the duct wall failure occurred at about 0.3 s after all of the pins disrupted finally and the fuel/steel mixture was formed, the present result indicates the possibility of early duct wall failure due to effects of molten steel in the mixture pool.

4.2.5 Effect of steel droplet size

In the above parametric cases, solid fuel, liquid fuel and liquid steel were homogeneously mixed in the pool with initial random configuration of numerical particles, of which size was equivalent to 1 mm square in the present 2D simulations. Therefore, the minimum size of dispersed phases in the pool can be also 1 mm square. Since this size could change heat transfer behavior, an additional parametric simulation was performed to investigate the effect of molten steel dispersion in the mixture pool using larger smaller steel droplets. In this case, steel droplets of 5 mm in width, each of which consists of 21 numerical particles, were mixed with fuel in liquid and solid phases. Therefore, the steel droplets dispersed coarsely in the mixture pool compared with other cases. Although the initial area fraction of molten steel-wall contact was 30% in the upper pool region, the other initial conditions were the same as those in Case A. **Figure 16** shows the initial material configurations in the case of larger steel droplets. It is noted that the initial contact area between molten steel and duct wall was exactly similar to that in Case A.
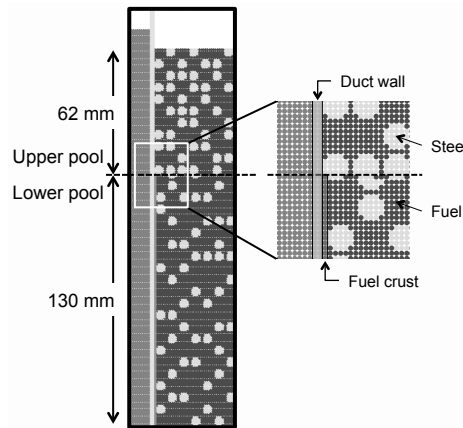

Fig. 16 Initial material configurations in the case of larger steel droplets.

The axial distributions of heat flux through the duct wall at 0.1 s, 0.3 s, 0.5 s and 0.7 s in the case of larger steel droplets is shown in **Fig. 17**. It can be seen that the heat flux distributions are similar to those in Case A, which is shown in **Fig. 8** (a). **Figure 18** compares the time variations of averaged heat fluxes over the upper and lower pool regions between Case A and the case of larger steel droplets. There is no essential difference between them. These results demonstrate that the coarse mixing of steel droplets in the pool does not change the heat transfer characteristics, although the heat transfer area between steel and fuel is smaller than that in Case A.
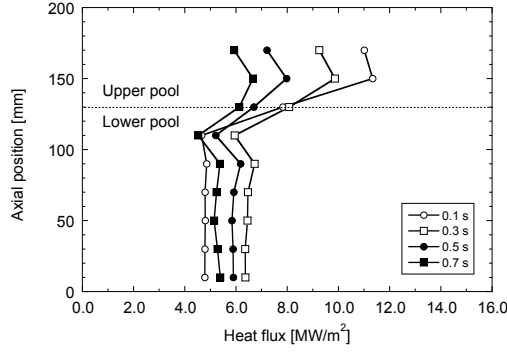
Fig. 17 Axial distributions of spatial average heat fluxes in the case of larger steel droplets.
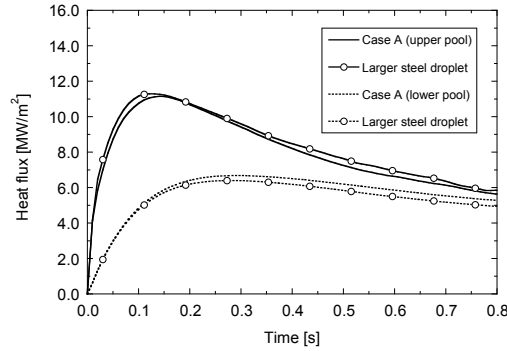

Fig. 18 Comparison of upper- and lower-pool heat fluxes between Case A and the case of larger steel droplets.

5.   Discussion

The potential thermal load to the duct wall should be caused by the heat transfer due to the temperature difference between the wall and the mixture pool, and the nuclear heating in the fuel. Therefore, the possible heat flux to the duct wall can be expressed by

$$q_{wall} = h_{eff}\Delta T + q_{nucl} \tag{29}$$

where h_{eff} is the effective heat transfer coefficient, which includes both conductive and convective effects, ΔT is the temperature difference between the duct wall surface and the bulk of mixture pool, and q_{nucl} is the heat flux caused by the nuclear heating in the fuel. It is noted that the direct heat transfer to the wall caused by the nuclear heating is possible without undergoing heat transfer processes among the pool materials.

As we discussed in Chapter 3, about half the fuel in the mixture pool is estimated in solid phase at the start of the pool-wall heat transfer. It is expected that the convection flows in the mixture pool might not develop largely in a short period of time. This might be bone out by the simulation result on solid fraction in fuel. **Figure 19** shows the time variation of solid-phase volume fraction in fuel in Case A. As discussed in Section 4.1, its initial faction is set to 47%. After the start of molten pool-wall heat transfer, part of molten fuel freezes into solid phase due to cooling by sodium through the duct wall and heat transfer to the colder pool materials. It can be seen from **Fig. 19** that the solid fraction reaches to 77% at 0.15 s, and gradually decreases due to the nuclear heating in the fuel. This large solid fraction might hider the fluid movement due to small mobility

of fuel material in the mixture pool during the early stage of pool-wall heat transfer. Therefore, we assume that development of convection flows is not enough to enhance the bulk heat transfer before the duct wall failure and contribution of convective heat transfer to the total heat flux becomes relatively smaller than others. On the other hand, the conductive heat transfer from the bulk of mixture pool to the duct wall can be enhanced by the molten steel mixed with fuel in the pool. If the mixture pool consists of the molten fuel and steel, we can simply estimate h_{eff} as

$$h_{eff} = \frac{k_m}{L/2} \tag{30}$$

where k_m is the effective thermal conductivity of the pool mixture and L is the pool characteristic length for heat transfer. The value of k_m was evaluated approximately using the following conventional Maxwell-Garnett's model[14], although it is applicable to dilute solid-liquid mixtures of relatively large particles:

$$k_m = \frac{k_s + 2k_f + 2(k_s - k_f)\alpha}{k_s + 2k_f - (k_s - k_f)\alpha} k_f \tag{31}$$

where k_f and k_s are the thermal conductivity of fuel and steel, respectively, and α is the volume fraction of steel in the mixture. By taking ΔT = 2,430 K as the initial temperature difference between the molten fuel and the duct wall, L = 0.04 m as the pool width, k_f = 5.0 W/(m·K) and k_s = 20.6 W/(m·K), the potential heat flux caused by the temperature difference between the wall and the mixture pool is estimated as 0.97 MW/m^2 for α = 0.33 and 1.5 MW/m^2 for α = 0.66. These values are fairly smaller than the calculated heat flux, which can be more than 10 MW/m^2 in the upper pool region. The present rough estimation suggests that enhancement of conductive heat transfer due to molten steel with high thermal conductivity has a relatively smaller contribution to such high heat flux.
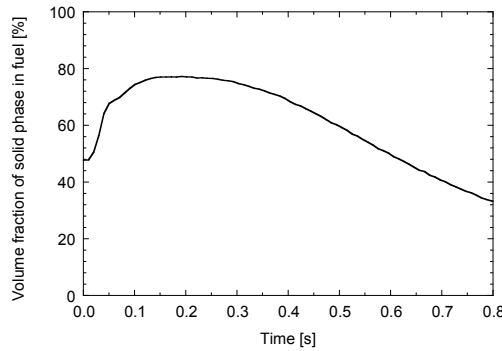

Fig. 19 Time variation of solid-phase volume fraction in fuel in Case A.

According to the above discussion, it is deduced that the thermal load to the duct wall is mainly induced by the nuclear heating in the fuel, and that the convective and conductive heat transfers from the bulk to the duct wall contribute less to it. This is demonstrated by the simulation case with coarse mixing of steel droplets in the mixture pool, where the steel droplet size had less effect of pool-duct heat transfer as presented in Section 4.2. On the other hand, the nuclear heat in the fuel can be effectively transferred thought the local contact of liquid steel to the duct wall. Therefore, larger contact area between the molten steel and the duct wall can enhance the local heat transfer

near the duct wall. This might be the main mechanism of effective heat transfer with high heat flux to the duct wall, which is caused by the molten steel in the mixture pool. In the upper pool region, although the fuel crust can be formed on the cold duct wall surface, it develops discretely due to relatively larger fraction of molten steel there, and hence the molten steel contact to the duct wall is not prevented largely. This mechanism is also attributed to one of the molten steel effects, which enhance the pool-duct heat transfer.

6.   Conclusions

In this study, fully Lagrangian simulations based on the finite volume particle method for multi-component, multi-phase flows were performed to analyze a set of heat transfer processes after the formation of fuel/steel mixture pool in the EAGLE in-pile ID1 test. The simulation methods used for the analyses can represent key thermal hydraulic behaviors involved in local thermal attack of the pool mixture to the duct wall, fuel crust formation on the wall surface and so on without empirical models such as flow regime map and heat-transfer correlations. Mechanisms of effective heat transfer from the molten pool to the duct wall were clarified through parametric simulations on material distribution in the molten pool after its formation. The simulation results indicate that effective pool-to-duct wall heat transfer is caused by local contact of molten steel with high thermal conductivity to the duct wall. As a result, the duct wall is exposed by large thermal load with heat flux more than 10 MW/m^2, which is driven by nuclear heat in the fuel. In addition, although the molten fuel can freeze on the duct wall surface as crust, it would not deteriorate the pool-to-duct wall heat transfer largely due to its local and discrete formation. The present results ensure a better phenomenological understanding of the duct wall failure leading to early fuel discharge from a fuel subassembly with an inner duct structure (FAIDUS), which is the design measure to prevent severe re-criticality events during core disruptive accidents of a sodium-cooled fast reactor.

Acknowledgements

Nomenclature

a	heat transfer area per unit volume [m^{-1}]
c_B	model parameter for buoyancy [–]
$\bar{f}$	volumetric force [N/m^3]
$\bar{f}_g$	gravity force per unit volume [N/m^3]
$\bar{g}$	gravity [m/s^2]
h	heat transfer coefficient [W/(m^2·K)]
h_{eff}	effective heat transfer coefficient [W/(m^2·K)]
H	specific enthalpy [J/kg]
H_f	specific latent heat of fusion [J/kg]
k	thermal conductivity [W/(m·K)]
k_f	thermal conductivity of fuel [W/(m·K)]

k_m	thermal conductivity of mixture pool [W/(m·K)]
k_s	thermal conductivity of steel [W/(m·K)]
L	pool characteristic length for heat transfer [m]
m	mass [kg]
$\bar{n}$	unit vector [–]
p	pressure [Pa]
q_{nucl}	heat flux caused by nuclear heating [W/m^2]
q_{wall}	heat flux to duct wall [W/m^2]
Q	volumetric heat source [W/m^3]
Q^h	heat transfer rate per unit volume at interface [W/m^3]
Q^m	energy transfer rate per unit volume due to phase change [W/m^3]
Q^n	volumetric heat source due to nuclear heating [W/m^3]
Q^I	net heat flow rate at interface [W/m^3]
$\bar{r}$	particle position [m]
r_e	cut-off radius [m]
R	radius of control volume [m]
S	surface of control volume [m^2]
t	time [s]
T_0	reference temperature [K]
T^I	interface temperature [K]
T^N	interface temperature without phase change [K]
$\bar{u}$	velocity [m/s]
V	control volume [m^3]

Greek Letters

α	volume fraction of steel in mixture [–]
β	volumetric thermal expansion coefficient [K^{-1}]
δ	crust thickness [m]
Δl	initial particle distance [m]
ΔS	interaction surface [m^2]
ΔT	temperature difference [K]
ϕ	arbitrary scalar function [–]
ϕ_{sur}	function value on the surface of control volume [–]
$\Gamma_{freezing}$	freezing rate per unit volume [kg/(m^3·s)]
$\Gamma_{melting}$	melting rate per unit volume [kg/(m^3·s)]
μ	viscosity [Pa·s]
ρ	density [kg/m^3]
ω	kernel function [–]

Subscripts

i	particle i
ij	between particles i and j
j	particle j
L	liquid

Liq   liquidus
M(i)   martial that constitutes of particle i
S   solid
Sol   solidus

References

1) H. Endo, S. Kubo, et al.: Elimination of Recriticality Potential for the Self-Consistent Nuclear Energy System, Prog. Nucl. Energy, Vol.40, No.3/4, pp.577-586 (2002).

2) I. Sato, Y. Tobita, et al.; Safety Strategy of JSFR Eliminating Severe Recriticality Events and Establishing In-Vessel Retention in the Core Disruptive Accident, J. Nucl. Sci. Technol., Vol.48, No.4, pp.556-566 (2011).

3) K. Konishi, J. Toyooka, et al.: Progress in Establishment of the Innovative Safety Logic for SFR Eliminating the Recriticality Issue with the EAGLE Experimental Program, Int. Scientific-Practical Conf. "Nuclear Power Engineering in Kazakhstan," Kurchatov, Kazakhstan, June 11-13, 2008 (2008).

4) J. Toyooka, K. Kamiyama, et al.: SIMMER-III Analysis of EAGLE-1 In-pile Tests Focusing on Heat Transfer from Molten Core Material to Steel-Wall Structure, Proc. 7th Korea-Japan Symposium on Nuclear Thermal Hydraulics and Safety (NTHAS7), Chuncheon, Korea, Nov. 14-17, 2010, N7P0058 (2010).

5) J. Toyooka, H. Endo, et al.: A Study on Mechanism of Early Failure of Inner Duct Wall within Fuel Subassembly with High Heat Flux from Molten Core Materials based on Analysis of an EAGLE Experiment Simulating Core Disruptive Accidents in an LMFBR, Transactions of the Atomic Energy Society of Japan, Vol.12, No.1, pp.50-66 (2013), [in Japanese].

6) K. Yabushita, S, Hibi: A Finite Volume Particle Method for an Incompressible Fluid Flow, Proc. Comput. Eng. Conf., Vol.10, pp.419-421 (2005), [in Japanese].

7) S. Zhang, K. Morita, et al.: A New Algorithm for Surface Tension Model in Moving Particle Methods, Int. J. Numer. Methods in Fluid, Vol.55, No.3, pp.225-240 (2007).

8) L. Guo, Y. Kawano, et al.: Numerical Simulation of Rheological Behavior in Melting Metal Using Finite Volume Particle Method, J. Nucl. Sci. Technol., Vol.47, No.11, pp. 1011-1022 (2010).

9) R.S. Mahmudah, M. Kumabe, et al.: 3D Simulation of Solid-Melt Mixture Flow with Melt Solidification Using a Finite Volume Particle Method," J. Nucl. Sci. Technol., Vol.48, No.10, pp. 1300-1312 (2011).

10) N. Shirakawa, Y. Yamamoto, et al.: Analysis of Subcooled Boiling with the Two-Fluid Particle Interaction Method, J. Nucl. Sci. Technol., Vol.40, No.3, pp.125-135 (2003).

11) R. Clif, J.R. Grace, et al.: Bubbles, Drops, and Particles, Academic Press, New York (1978).

12) K. Konishi, S. Kubo, et al.: The EAGLE Project to Eliminate the Recriticality Issue of Fast Reactors -Progress and Results of In-pile Tests-," Proc. 5th Korea-Japan Symposium on Nuclear Thermal Hydraulics and Safety (NTHAS5), Jeju, Korea, Nov. 26-29, 2006, NTHAS5-F001 (2006).

13) International Atomic Energy Agency (IAEA), Thermophysical Properties of Materials for Nuclear Engineering: A Tutorial and Collection of Data, Vienna, Austria, IAEA-THPH (2008).

14) J. Lee, S. Lee, et al.: A Review of Thermal Conductivity Data, Mechanisms and Models for Nanofluids, Int. J. Macro-Nano Scale Transport, Vol.1, No.4, pp.269-322 (2010).